Renewable Energy 229 (2024) 120686

Contents lists available at ScienceDirect

Renewable Energy

journal homepage: www.elsevier.com/locate/renene

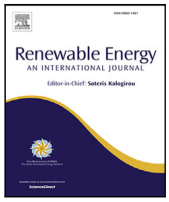

The role of size and inertia on the hydrodynamics of a self-reacting heave single point absorber wave energy converter

Gianluca Zitti *, Maurizio Brocchini

Dipartimento di Ingegneria civile Edile e Architettura, -università politecnica delle Marche, via Brecce Bianche 12, ancona, 60131, Italy

ARTICLE INFO

Keywords:
Wave energy converter
Self-reacting floating point absorber
Nonlinearity
Wave overtopping
Out-of-water motion
Computational fluid dynamics

ABSTRACT

We propose a detailed numerical study of a self-reacting floating point absorber, resembling the Ocean Power Technologies device PB3 PowerBuoy, for a possible installation in the Adriatic Sea. A simplified model of the mentioned device, composed of a floater sliding along a reacting body, which supports the floater, is studied, reproducing and analysing the most complex nonlinear phenomena, such as the wave overtopping and the out-of-water motion of the floater. Three different sizes of the device have been simulated, each with three different masses of the floater, deriving the time evolution of the wave in the surrounding of the floater, its frequency dispersion and energy content, the generated exciting force, the wave overtopping over the floater, and the out-of-water motion of the floater. The results highlight that the linear response is favoured by small floater density and optimal floater thickness. Additionally, large-sized devices are characterized by linear, but dissipative, response, while the response of medium-sized devices is only apparently linear.

1. Introduction

The extraction of renewable energy from waves in seas and oceans constitutes a huge potential resource of renewable energy, which is very little exploited, in spite of the large number of proposed devices [1–6]. This is due to the relatively immature development of wave energy harvesting and to the lack of a dominant technology [7]. Most prototypes of wave energy converters (WECs) has been tested in the most energetic seas, like the North Sea, but recently the Mediterranean Sea has been identified as a strategic location for the development and field test of innovative WECs [8–15].

The Adriatic Sea is characterized by a large number of infrastructures, including a number of offshore platforms that have reached the end of their lives and requires to be dismantled. However, the ecological impact and the economic investments for their complete dismantling is pushing toward a partial removal and/or reuse of offshore platforms [16–22]. In particular, the European project Place [23] proposed a combination of technologies and solutions for the eco-sustainable reuse of offshore platforms, to support multifunctional activities in the Blue Growth sector. These activities require a supply of energy that, in the offshore environment, can be provided through WECs.

The highest technology-readiness level WEC deployed offshore in the Adriatic Sea is the Ocean Power Technologies PB3 Powerbuoy (OPT PB3 hereafter),[1] within the ENI's Clean Sea initiative [24,25], which has been considered for an additional possible installation in the Adriatic sea, close to the Viviana platform [42.656403 *N* 14.155051 E]. The OPT PB3 is a Self-Reacting two-body Floating Point Absorber (SRPA), which is composed of two buoyant, free-surface piercing bodies: the floater, characterized by the larger motion due to waves, and the reacting body, which supports the floater and ensures the stationing and stability of the entire device.

The design optimization of the OPT SRPA has been carried both by the developer, by means of extensive wave tank and periodic ocean testing of their PowerBuoy wave energy converter, and by researchers [26]. In particular, Beatty et al. [27,28] compared the power production of different geometries and configurations of SRPA devices, using both boundary element method simulations and experimental tests. The main reference for the study of SRPA is the third reference model (RM3) of wave energy converter developed by The U.S. Department of Energy, The National Renewable Energy Laboratory (NREL), and The Sandia National Laboratory. Even if it is widely studied in literature [29–33], it is significantly larger than the OPT PB3 installed in the Adriatic sea. As a reference, we point out that the RM3's floater diameter is 20 m, while the floater diameter of the PB3 installed in the Adriatic sea is 2.65 m.

The aim of this work is to investigate the nonlinearities that may arise during the interaction of the floater of a PB3 with waves, and how the size and mass of the floater can affect them. To limit the

* Corresponding author.
E-mail address: g.zitti@staff.univpm.it (G. Zitti).

[1] http://www.oceanpowertechnologies.com

https://doi.org/10.1016/j.renene.2024.120686
Received 23 November 2023; Received in revised form 15 May 2024; Accepted 19 May 2024
Available online 21 May 2024

computational effort without sacrificing the simulation of hydrodynamics, the geometry of the device has been simplified, modelling the reaction part as a fixed pile and the floater as a simple disk not separated by the pile. We use a fully-nonlinear computational fluid-dynamics (CFD) methodology to study the heave response of a PB3-type SRPA, considering a possible installation in the Adriatic Sea and focusing on the nonlinear phenomena of the fluid–structure interaction. Compared to other methods used for modelling floating wave energy converters, such as the radiation/diffraction models, the fully-nonlinear CFD is capable of reproducing nonlinear phenomena minimizing the parametrization of the physical processes, even if some simplifications are necessary to limit the computational cost and avoid numerical divergences. In addition, compared with laboratory experiments, CFD evaluates the hydrodynamic results with high resolution in space and time, allowing for an almost continuous tracking of the free surface in space and time.

The hydrodynamics of an oscillating body in viscous oscillatory flows, in an assigned location, is governed by the Reynolds number $Re = UD/\nu$ and Keulegan–Carpenter number $KC = UT/D$, which can be lumped into the unique parameter $\beta = Re/KC = D^2/\nu T$ [34], where D is the characteristic length of the body, ν is the fluid kinematic viscosity, while U and T are the characteristic velocity and period of the oscillatory flow. Xu et al. (2019) [32] showed that the viscous effects can be correctly described using Re and KC, unless the wave frequency is equal or lower than the resonance frequency of the device. In this case additional nonlinear effects are generated by the wave overtopping and by the out-of-water motion of the device. With out-of-water motion we mean the chance that the bottom surface of the floater is not fully immersed, even for a small amount of time.

The use of CFD allowed us to evaluate the quantities associated to the wave overtopping and the out-of-water motion of the floater, and to compare these nonlinear quantities with the hydrodynamic parameter describing the nonlinear response of the floater, such as the response amplitude operator. The wave overtopping and the out-of-water motion of the device can be influenced by the floater freeboard and the floater draft, which are evaluated balancing the weight force and the buoyancy force of the floater in a steady floating condition. The derived dimensionless freeboard is:

$$R_f^* = \frac{H_{fl}}{H_w}\left(1 - \frac{\rho}{\rho_w}\right), \tag{1}$$

while the dimensionless draft is:

$$R_d^* = \frac{H_{fl}}{H_w}\frac{\rho}{\rho_w}, \tag{2}$$

where H_{fl} is the height of the floater, ρ is the floater density, ρ_w is the water density, and the wave height H_w is used as length scale.

To investigate these nonlinear phenomena, we numerically simulated the interaction of devices with different characteristic lengths and different masses with a linear wave representative of the Adriatic Sea operating condition, characterized by wave height $H_w = 1$ m and wave period $T_w = 5.07$ s, varying independently the characteristic length and characteristic mass of the floater, since they directly affect the dimensionless numbers Re, KC, R_f^* and R_d^*.

Summarizing, the aim of this work is the study and parameterization of nonlinear phenomena that characterize the working of a PB3-type SRPA WEC. After the description of the fully-nonlinear model used for our study in Section 2, the main nonlinearities of the wave-device interaction and of the floater dynamics are detailed and described in Section 3. In Section 4 the nonlinear responses are compared with the varied parameters and the measured nonlinear phenomena, finding how the density, size and mass of the floater affect the linearity of the response. To our knowledge, this is one of the rare studies that provides insight into how the device geometry and inertia can be used to optimize the linear response of the WEC. Closing remarks are reported in Section 5.

2. Methods:numerical model of the PB3-type SRPA

To contain the computational cost, most of the studies on SRPA are based on the application of the diffraction/radiation theory in the frequency domain, where the boundary element method is proposed to predict numerically the hydrodynamic parameters of a two-body FPA. These models are fundamental for the study, design and control of the Power Take Off system, as stated in several literature studies [35–37]. However, they entail the parametrization of some nonlinear phenomena.

On the other hand, Volume Of Fluid (VOF) CFD models, able to reproduce the nonlinear phenomena due to the interaction of the device with the fluid, are rarely used due to their computational cost and to the difficulty to manage the boundary condition at the sliding surface between the float and the reacting body. An accurate CFD modelling of a two-body, self-reacting floating point absorber was proposed by Yu et al. (2013) [29], showing that Reynolds Averaged Navier Stokes (RANS) simulations agreed with the experimental data. In particular, the numerical simulations, validated with the experimental results described in Li et al. (2011) [38], revealed that the nonlinear interaction between waves and the RSPA device increase with the increase of wave height, because of the larger wave overtopping and the re-entering impact of the out-of-water float. In Yu et al. (2013) [29], the numerical issue of the two adherent bodies was solved by separating the device into two parts not touching each other: an upper float and a fully submerged reaction section. The same approach was used in Xu et al. (2019) [32], showing that nonlinear effects are particularly significant when the wave height is large and the period is near or shorter than the resonant period of the RSPA system.

For the study of the nonlinear behaviour of a SRPA, a three-dimensional RANS-VOF CFD model is here used, implemented through the commercial software ANSYS Fluent. As a novelty, instead of splitting the device into two bodies separated by a gap, the device is modelled by two attached parts: a vertical slender pile with diameter D_p, representing the reaction part of the RSPA, and a floating disk with diameter D_{fl} and height H_{fl}. To contain the computational effort, the reacting pile is assumed fixed, while the floating disk is allowed to move in the heave direction only. This simplification moves us away from the simulation of a self-reacting two-body point absorber, and towards the modelling of heaving single-body point absorber. However, it allows us to accurately simulate the hydrodynamics in the surrounding of the floater, which is the focus of our work.

The geometry of the domain, the mesh size and the size of the time step of the numerical discretization were chosen to optimize the numerical simulation and limit the computational cost. The numerical domain is a three dimensional box 25 m tall, 35 m long (stream-direction) and 20 m wide. The support pile axis is located in the middle of the tank, 10 m from the inflow boundary. A sketch of the studied geometry is reported in Fig. 1.

The forcing wave is simulated exploiting the two phase RANS-VOF open channel flow model of ANSYS Fluent, with compressible air (with reference density $\rho_a = 1.225$ kg/m^3), incompressible water (with density $\rho_w = 998.2$ kg/m^3) and volume fraction cutoff of 10^{-6}. The inflow boundary condition is defined with a flow field derived from a Stoke's wave theory, characterized by the still-water depth $h = 21$ m, wave height $H_w = 1$ m and wave length $\lambda = 40$ m, corresponding to the wave period $T_w = 5.07$ s, which is representative of a frequent wave in the Adriatic sea in the location of the Viviana platform.

At the outflow boundary and at the upper boundary, a gauge pressure condition is assigned, based on the location of the free surface. A numerical beach, which adds a sink dissipative term to the momentum balance of the cells next to the outflow boundary, has been used to remove the numerical reflection of the wave. The no-slip boundary condition is used at the sea bottom, for the support pile and for the moving floater, while a free-slip boundary condition is used for the lateral sides of the domain.

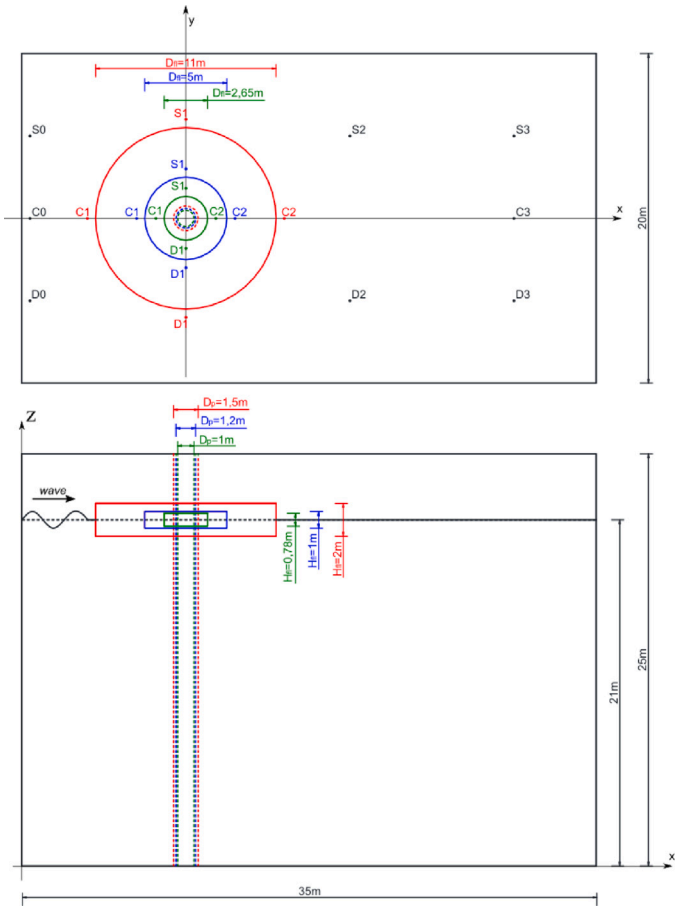

Fig. 1. Geometry of the numerical model, with location of the floater (coloured lines), of the support pile (coloured dashed lines) and of the gauges C_i, S_i and D_i, as defined in Table 2. The three different geometries of the SRPA (and the corresponding different locations of the gauges) are reported with three different colours.

The boundary walls of the floater are allowed to move in the heave direction, following the dynamic law:

$$M\ddot{z}_{fl}(t) + kz_{fl}(t) = F_{fl}(t) \tag{3}$$

where z_{fl} is the vertical displacement of the floater, $F_{fl}(t)$ is the resultant of both pressure and shear stresses acting on the floater boundaries, and M is the mass of the floater. Since the focus of the paper is not the evaluation of the extracted energy as function of the PTO characteristics, but the understanding of the nonlinear response of the floating part, the PTO has not accurately modelled but a linear elastic internal reaction, with coefficient $k = 10^5$ N/m, has been added. This allows us to identify a specific frequency of such internal reaction, representative of the PTO, defined as $f_{int} = \frac{\sqrt{k/M}}{2\pi}$.

A mesh of linear tetrahedical cells is generated with the ANSYS Meshing Tool (ICEM CFD), with maximum edge size 0.2 m in the surrounding of the boundary walls and 0.4 m elsewhere. An unstructured mesh is used to facilitate the remeshing at each time step, which is necessary to simulate the displacement of the floater. A frame of the updated mesh in the surrounding of the floater is illustrated, as an example, in Fig. 2, while a video of the mesh evolution is available in the Supplementary Materials.

The numerical pressure-based model [39] solves the discretized form of the RANS equation, including the Menter's k-ω Standard model. Due to the presence of a large moving body in the domain, a partial equilibrium of both pressure gradient and body forces is taken into account, to facilitate the convergence of the solution. The equations are discretized in space according to the computed mesh and in time

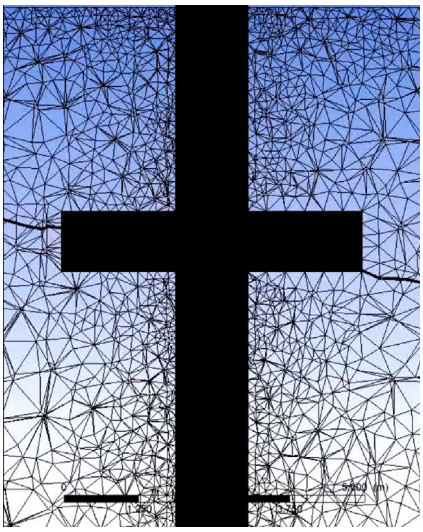

Fig. 2. A detail of the mesh in the surrounding of the floater for test M6574, in a vertical section along the direction of wave propagation.

using a time step of $\Delta t = 0.005$ s. They are then solved using an iterative Semi-Implicit Method for Pressure Linked Equations-Consistent, until a residual error of less than 10^{-3} for the mass balance equation, 10^{-5} for the momentum balance equation, 10^{-3} for kinetic energy, 10^{-3} for turbulent energy dissipated, and 10^{-3} for the volume fraction predicted in the two-phase method is reached, or until 250 iterations are performed for each time interval. Each simulation is run for a total time of 30 s, *i.e.* at least five wave periods.

At each time step, the displacement of the floater is evaluated solving the differential Eq. (3), the location of the floater is updated and the mesh affected by the motion, located along the pile boundary and inside the domain, is remeshed exploiting the spring-based smoothing mesh-update method [39].

Three different sizes of the RSPA have been simulated, each with three different masses of the floater, obtaining the nine tests reported in Table 1. The smallest size, characterized by a floater diameter of D = 2.65 m, and the smallest floater density are inspired to the PB3 system currently installed in the Adriatic sea, while the largest size has been derived from the literature [29,35]. The intermediate configuration has been defined accordingly, to have different degrees of buoyancy.

3. Results

This section gives separately the results for the hydrodynamics of the waves in the surrounding of the SRPA floater, and for the dynamics of the floater interacting with them. The Fast Fourier transform is used to identify the linear and nonlinear contributions. Finally, the overtopping of the wave over the floater and the volume of air under the floater are quantified, as sources of possible nonlinearities.

3.1. Wave characterization

The interaction of the inflow wave with the fixed and moving walls of the modelled SRPA generates a change of the wave characteristics. For this reason, waves have been sampled at several different locations close to the inflow boundary, in the surrounding of the floater and downstream of the device, in the location of the gauges shown in Fig. 1 and reported in Table 2.

The water elevation at each gauge is evaluated numerically integrating the volume fraction of water α_w in the vertical direction within

Table 1
Geometrical and Inertial characterization of the numerical simulations.

ID	D_{fl} [m]	H_{fl} [m]	D_p [m]	V_{fl} [m^3]	M [kg]	ρ [kg m^{-3}]	Re	KC	β	R_f^*	R_d^*	f_{int}
L32700	11	2	1.5	186.53	32 700	175	4.34E+06	0.18	2.39E+07	0.831	0.169	0.278
L65400	11	2	1.5	186.53	65 400	351	4.34E+06	0.18	2.39E+07	0.662	0.338	0.197
L130800	11	2	1.5	186.53	130 800	701	4.34E+06	0.18	2.39E+07	0.323	0.677	0.139
M3240	5	1	1.2	18.50	3240	175	1.97E+06	0.40	4.93E+06	0.422	0.078	0.884
M6475	5	1	1.2	18.50	6475	350	1.97E+06	0.40	4.93E+06	0.344	0.156	0.625
M9250	5	1	1.2	18.50	9250	500	1.97E+06	0.40	4.93E+06	0.277	0.223	0.523
S584	2.65	0.78	1	3.69	584	158	1.05E+06	0.75	1.39E+06	0.344	0.046	2.083
S1168	2.65	0.78	1	3.69	1168	317	1.05E+06	0.75	1.39E+06	0.297	0.093	1.473
S1818	2.65	0.78	1	3.69	1818	493	1.05E+06	0.75	1.39E+06	0.245	0.145	1.180

Table 2
Coordinates (in m) of the location of the gauges for the evaluation of the wave source.

Gauge		D0	C0	S0	D2
All tests	x [m]	−9.50	−9.50	−9.50	10.00
	y [m]	−5.00	0.00	5.00	−5.00
Gauge		S2	D3	C3	S3
All tests	x [m]	10.00	20.00	20.00	20.00
	y [m]	5.00	−5.00	0.00	5.00
Gauge		D1	C1	S1	C2
Tests L	x [m]	0.00	−6.00	0.00	6.00
	y [m]	−6.00	0.00	6.00	0.00
Tests M	x [m]	0.00	−3.00	0.00	3.00
	y [m]	−3.00	0.00	3.00	0.00
Tests S	x [m]	0.00	−1.825	0.00	1.825
	y [m]	−1.825	0.00	1.825	0.00

the domain, and subtracting the initial still water depth h:

$$\eta(x,y) = \int_{0m}^{25m} \alpha_w(x,y,z)\,dz - h \tag{4}$$

The obtained wave amplitudes have been analysed using a fast Fourier transform (FFT) algorithm implemented in the MATLAB Software, finding out that all the measured waves are characterized by the same peak frequency of the inflow wave $f \sim 0.2$ Hz, even if in some cases, minor secondary peaks are present at the second harmonic frequency, given by some minor reflection at the walls (see Figures from S1 to S9 of the Supplementary Material for confirmations). The changes in space of the main spectral peak with respect to the inflow wave main spectral peak (sampled at probe C0) are summarized in Table 3.

These results show that in many locations the main spectral peak is reduced by the interaction with the floater, because of energy dissipation, even if at specific locations of some tests the main spectral peak is increased. As an example, in several tests with the higher density (S1818, L65400 and L130800), the waves probed in front and on either lateral side of the floater show a slight increase in the main peak. The largest decrease in the main peak is located just downstream of the floater (see gauge C2 for every test), as expected. However, such an expected reduction varies in wide ranges: 25%–50% for S tests, 75%–80% for M tests and 10%–30% for L tests. Other changes depend on the specific interactions that the wave has with each type of floater.

An important property for the evaluation of the SRPA fluid–structure interaction is the wave source, evaluated as the wave flux at a specific location:

$$J = \int_{0m}^{25m} \alpha_w\,(p_d u)\,dz \tag{5}$$

where u is the streamwise velocity and p_d is the dynamic pressure evaluated as $p_d = p + \rho_w g(z-h)$, being p the total pressure and g the gravitational acceleration. Using Eq. (5), the wave source has been evaluated at the different locations of the gauges shown in Fig. 1 and reported in Table 2. The wave source has been made dimensionless using the inflow wave source measured at gauge C0: $J^* = J/J_{C0}$. The time-averaged wave source, evaluated over a finite number of periods (at least four periods, neglecting the first ones to avoid transient phenomena) are illustrated in Figs. 3–5. Such results show that the large device reduces the wave source of at least 75%, regardless of its mass (see J^* at gauges C2 and C3 in Fig. 3). Instead, medium and small SRPAs (Figs. 4 and 5) reduce the wave source between 35% and 50%, again with no clear dependence from the mass. This suggests the wave source extraction and dissipation is affected by the size and not by the mass of the floater.

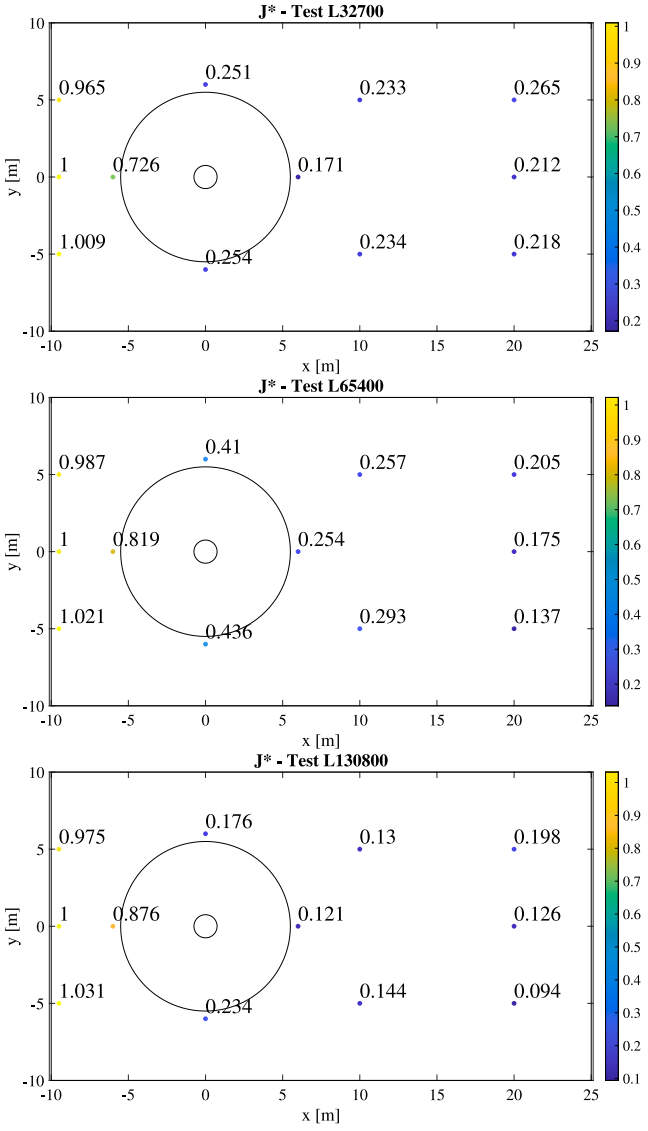

Fig. 3. Space distribution of the time-averaged dimensionless wave source for tests with large size SRPA.

Table 3
Variations in space of the spectral main peak with respect to the inflow wave spectral main peak (sampled at probe C0).

Gauge	S584	S1168	S1818	M3245	M6465	M9250	L32700	L65400	L130800
D0	0.987	0.982	0.989	0.970	0.969	0.950	0.999	0.882	0.791
C0	1.000	1.000	1.000	1.000	1.000	1.000	1.000	1.000	1.000
S0	0.992	0.990	0.983	0.989	0.981	0.950	0.872	0.706	0.590
D1	0.631	0.623	1.175	0.881	0.899	0.806	0.960	1.044	1.014
C1	0.905	0.914	1.508	1.258	1.304	1.145	1.653	1.697	1.479
S1	0.633	0.632	1.188	0.868	0.900	0.789	0.920	1.007	1.017
D2	0.863	0.862	1.117	0.988	1.122	0.882	1.256	1.220	0.980
C2	0.490	0.485	0.730	0.241	0.264	0.198	0.888	0.714	0.735
S2	0.944	0.943	1.197	0.944	1.065	0.830	1.200	1.107	0.792
D3	0.827	0.826	1.158	0.899	1.092	0.736	0.838	0.719	0.522
C3	0.851	0.846	1.206	0.847	1.147	0.748	0.809	0.788	0.601
S3	0.812	0.811	1.160	0.913	1.175	0.777	0.940	0.906	0.752

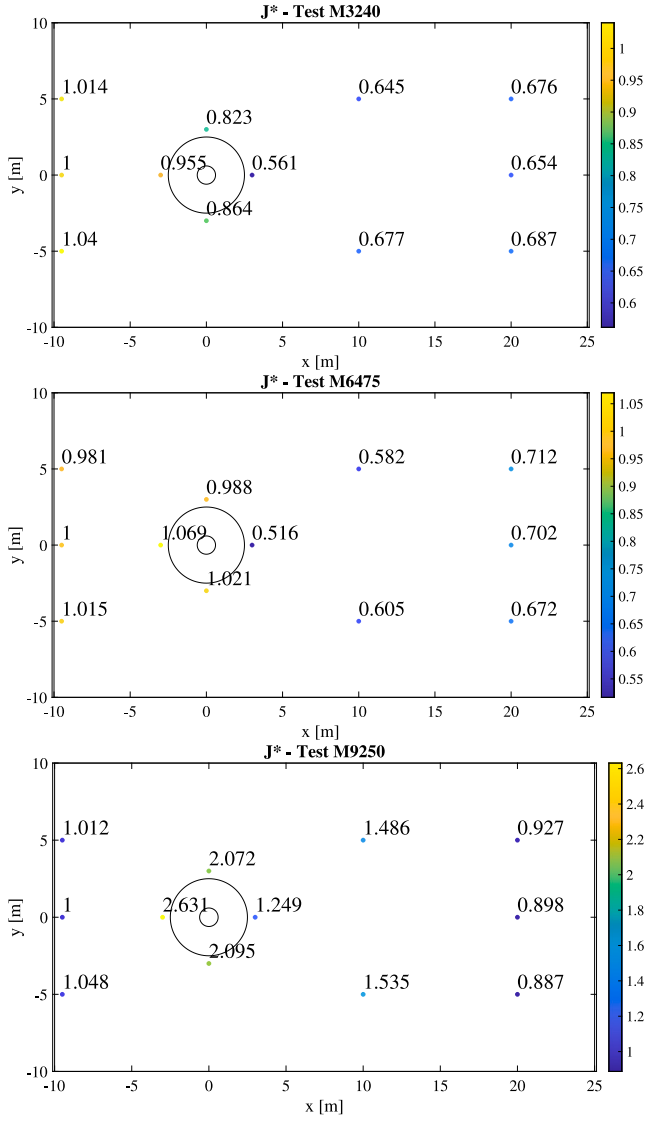

Fig. 4. Space distribution of the time-averaged dimensionless wave source for tests with medium size SRPA.

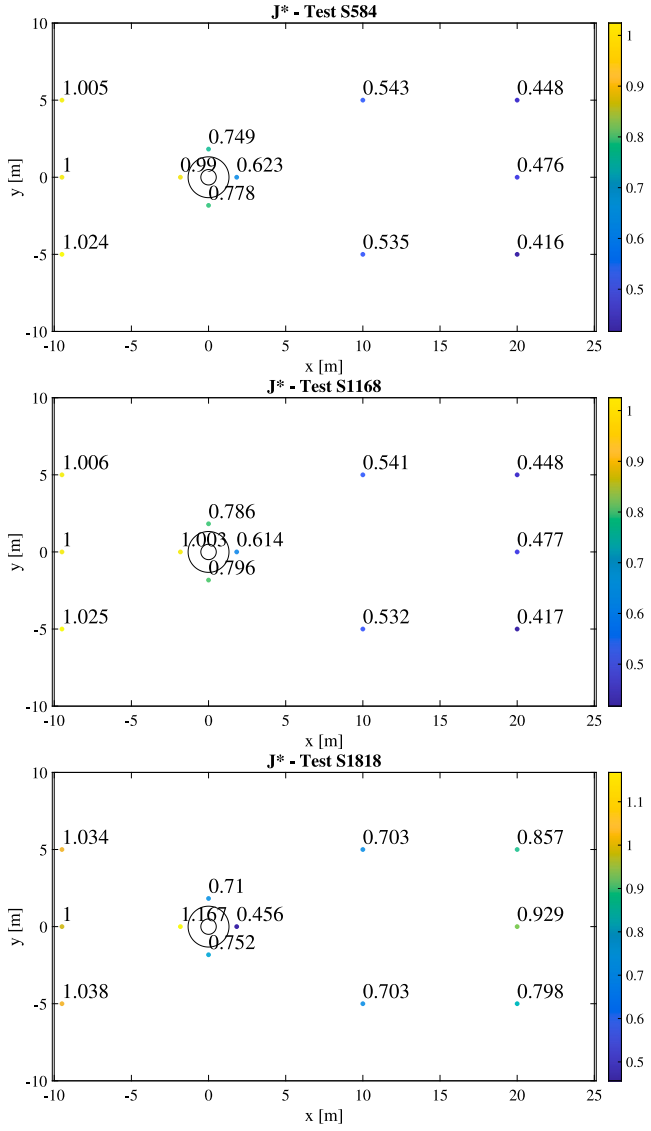

Fig. 5. Space distribution of the time-averaged dimensionless wave source for tests with small size SRPA.

In addition, the M9250 test shows a significant increase in wave source in front of the device (gauge C1 in the bottom panel in Fig. 4), which coincides with an increase in wave source also downstream of the device and suggests a peculiar interaction of the floater with the fluid. Such wave intensification in front of the floater is not unique, but also occurs for other tests with small and medium-sized floaters.

The wave source in front of the device increases with the mass for all SRPA sizes tested and differs from the unity for several tests, showing the wave undergoes significant changes during its interaction with the structure. In particular, large-size tests are all characterized by $J^* \leq 1$, *i.e.* in the case of large RSPAs there is always a dissipation of the wave source.

Table 4
Results of the frequency analysis for the floater displacement z_{fl}.

	$P(z_{fl})(f_0)$ [m]	$P(z_{fl})(f_w)$ [m]	$\Sigma_i P(z_{fl})(f_i)$ [m]	$NLRAO$	RAO
L32700	0.118	0.163	0.082	0.164	0.325
L65400	0.001	0.164	0.088	0.176	0.329
L130800	0.000	0.161	0.111	0.222	0.322
M3240	0.039	0.509	0.081	0.163	1.018
M6475	0.027	0.472	0.098	0.195	0.944
M9250	0.131	0.533	0.000	0.000	1.067
S584	0.357	0.383	0.052	0.103	0.766
S1168	0.026	0.382	0.031	0.063	0.764
S1818	0.022	0.400	0.259	0.519	0.800

Table 5
Results of the frequency analysis for the vertical force acting on the floater F_{fl}.

	$P(F_{fl})(f_0)$ [N]	$P(F_{fl})(f_w)$ [N]	$\Sigma_i P(F_{fl})(f_i)$ [N]	$NLRAO_F$ [N/m]	RAO_F [N/m]
L32700	388.1	164.9	62.8	125.50	329.7
L65400	537.1	160.4	50.0	99.98	320.7
L130800	905.6	131.5	101.7	203.41	263.0
M3240	34.11	2.42	0.77	1.54	4.83
M6475	62.71	0.00	4.45	8.90	0.00
M9250	87.12	0.00	4.56	9.12	0.00
S584	9.07	3.50	0.26	0.51	7.00
S1168	13.66	3.18	0.15	0.30	6.35
S1818	18.57	2.99	0.78	1.55	5.98

3.2. Floater dynamics

The features of interest for the analysis of the model dynamics are those reported in Eq. (3), *i.e.* the vertical displacement of the floater z_{fl} and the resultant of both pressure and shear stresses acting on it F_{fl}. The frequency analysis of these two features is executed with the FFT algorithm implemented in the MATLAB Software (see Figure S10 and Tables S1, S2 and S3 of the Supplementary Material for intermediate results) and Tables 4 and 5 summarize the results separating the following contributions:

- the spectral peak corresponding to the zero frequency $f_0 = 0$ Hz, *i.e.* a time-averaged position/force, which we can refer to an hydrostatic condition;
- the spectral peak corresponding to the frequency of the wave reproduced in the numerical simulation $f_w = 0.19$ Hz, from which it is possible to calculate the response amplitude operator (RAO) for both the floater displacement and force:

$$RAO = \frac{P(z_{fl})(f_w)}{P(\eta)(f_w)} \quad []; \quad RAO_F = \frac{P(F_{fl})(f_w)}{P(\eta)(f_w)} \quad [\mathrm{N/m}]; \tag{6}$$

- the sum of the remaining peaks (different from f_0 or f_w), representative of dispersion phenomena, from which the nonlinear response amplitude operator (NLRAO) is defined for both the floater displacement and force:

$$NLRAO = \frac{\Sigma_i P(z_{fl})(f_i)}{P(\eta)(f_w)} \quad []; \quad NLRAO_F = \frac{\Sigma_i P(F_{fl})(f_i)}{P(\eta)(f_w)} \quad [\mathrm{N/m}]; \tag{7}$$

The spectral displacement peak response corresponds to the characteristic frequency of the exciting waves for all the tests, *i.e.* the displacement response is dominated by linear dynamics. However, as the floater becomes larger, the displacement response spreads over a larger frequency range, *i.e.* nonlinear contributions to the displacement response of the floater increase. In contrast, the spectral force is dominated by the contribution in the characteristic frequency of the wave only for the small and large SRPA, while for the medium SRPA the second harmonic simulated with the second-order Stokes theory is dominant, $f \simeq 0.4$ Hz. In general, the nonlinear contributions vary with both size and mass in different manners for the displacement and force responses.

3.3. Floater overtopping and out of water motion

We now focus on a couple of nonlinear phenomena that could affect the motion of the device and induce the nonlinear responses we have highlighted in the previous paragraphs. The first phenomenon is the overtopping of the wave over the floater, which can be quantified using the volume:

$$V_{over} = \int_{S_{fl}} \left(\eta(x,y) - z_{top}\right) dxdy \tag{8}$$

where S_{fl} is the horizontal upper surface of the floater, z_{top} is its vertical position, and the water elevation η is evaluated as from Eq. (4). A sketch of the overtopping volume V_{over} is shown in Fig. 6. During the overtopping, the identified volume of water provides a downward force on the floater, affecting it dynamics.

The other phenomenon is the motion of the floater out of the water, when the wave's thrust on the floater decreases dramatically. The out-of-water motion of the floater is identified as the phase in which the lateral side of the floater is no more wet, and it is quantified by the volume of air below the floater, *i.e.* between the bottom surface of the floater and the free surface of the water:

$$V_{out} = \int_{S_{fl}} \left(z_{bottom} - \eta(x,y)\right) dxdy \tag{9}$$

where z_{bottom} is the vertical position of the lower surface of the floater. A sketch of such volume V_{out} is shown in Fig. 6. A non-zero value of V_{out} does not mean that the floater is flying out of the water, but that the surface subjected to the wave action decreases, this reducing the hydrostatic force.

These quantities are made dimensionless with the floater volume ($V^*_{over/out} = V^*_{over/out}/V_{fl}$) and the peaks of V^*_{over} and V^*_{out} have been identified by selecting local maxima with values larger or equal to 10% of the largest peak. The averaged values for each test are reported in Table 6 (see Figures S11 and S12 of the Supplementary Materials for intermediate results).

The overtopping volume V^*_{over} varies with both the size of the device and its mass: it decreases with increasing floater size (compare test S1168, with peaks of $V^*_{over} \sim 0.2$, test M6465, with peaks of $V^*_{over} \sim 0.1$ and test L65400, with peaks of $V^*_{over} \sim 0.03$, in Table 6), while an increasing dependence on the mass is evident for the tests with medium and small size (see the increasing value of V^*_{over} for small and medium test in Table 6). On the other hand, the peaks of V^*_{out} are negligible in the cases of large and medium-sized RSPAs, regardless of the mass/density.

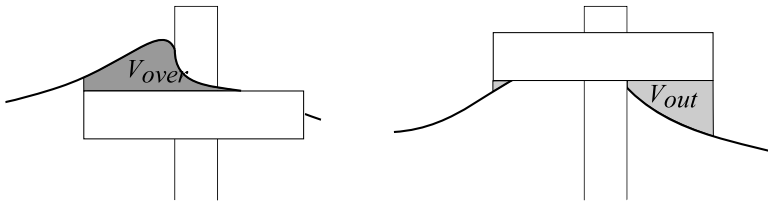

Fig. 6. 2D sketch of the Volume identified for the overtopping volume V_{over} (left panel) and for the volume of air under the floater V_{out} during the motion out of water (right panel).

Table 6
Average value of the peaks of the overtopping volume and of the volume of air under the floater, made dimensionless with the floater volume.

ID	V^*_{over}	V^*_{out}
L32700	0.047	0.003
L65400	0.028	0.000
L130800	0.064	0.000
M3240	0.080	0.004
M6475	0.095	0.004
M9250	0.102	0.002
S584	0.090	1.090
S1168	0.188	1.057
S1818	0.208	0.914

For the cases of small RSPAs the peaks are of the same size as the floater volume (see $V^*_{out} \sim 1$ in Table 6), with no particular dependence from the mass of the floater.

4. Discussion

The analysis of the nonlinear processes involved in the interaction between the incident wave and the device is not straightforward. In fact, several different regression functions have been tested, searching for a relation between the RAO, $NLRAO$ RAO^*_F, $NLRAO^*_F$, V^*_{out} and V^*_{over}, and the main RSPA dimensionless parameters shown in Table 1, but few regressions provides a coefficient of determination R^2 larger than 0.5.

The only effective regressions are found between the dimensionless force response amplitude operators, RAO^*_F and $NLRAO^*_F$, and the dimensionless freeboard R^*_f and draft R^*_d, respectively:

$$\begin{aligned} RAO^*_F &= 0.0031 R^*_f - 0.0005 \qquad R^2 = 0.57 \\ NLRAO^*_F &= 0.0019 R^*_d - 0.00004 \qquad R^2 = 0.79 \end{aligned} \tag{10}$$

being the RAO for the floater force made dimensionless using the scale $\Pi = \frac{\rho_w g V_{fl}}{D_{fl}}$, hence:

$$RAO^*_F = RAO_F/\Pi; \quad NLRAO^*_F = NLRAO_F/\Pi \tag{11}$$

The first result in Eq. (10), shown in the left panel of Fig. 7, states that an increasing relation exists between the force response amplitude operator and the freeboard of the floater, *i.e.* with the combination of the densities and dimensions given by Eq. (1). It follows that to increase the linearity of the response, it is necessary to minimize the density of the floater, or to increase the ratio H_{fl}/H_w. Assuming a given density, a thicker floater increases the linearity of the force response.

Reciprocally, the nonlinear response shows an increasing trend with the draft (see the second result in Eq. (10) and the right panel in Fig. 7). Considering the draft definition in Eq. (2), to reduce the nonlinearity we can reduce either ρ or H_{fl}. Taking into account the previous result concerning the linear response, it becomes clear that it is necessary to minimize the floater density in order to keep the response as linear as possible. Within the technological limits of this minimization, an optimal value of the floater thickness can be sought.

On the other hand, the RAOs calculated with our fully nonlinear model are different from those that can be obtained with potential models, such as the radiation-diffraction model implemented in the ANSYS AQWA software, which gives $RAO \simeq 1$ in most of the considered configurations (for confirmations, see the results reported in S4 of the Supplementary Materials). The RAOs obtained with the fully nonlinear model are similar to those obtained with the potential model only in the case of medium-sized SRPAs, suggesting that only this class of devices has a dominant linear response to the exciting wave, even if this class is not characterized neither by larger freeboard, nor by smaller draft.

However, if we perform a deeper analysis of the results, different additional considerations can be done. First of all, we notice that large devices induce a considerable drop of the forcing wave downstream the device (see $J^* \leq 0.25$ at downstream gauges in Fig. 3), while the wave source is only slightly reduced upstream the device (see $J^* \sim 0.7$–0.9 at the upstream gauge in Fig. 3). Such significant drop in the forcing wave does not correspond to an energy transfer to the device, as stated by the small response amplitude values (see $RAO \simeq 0.35$ and $NLRAO < 0.25$ for all large devices in Table 4). It follows that the energy is dissipated, but such dissipation does not influence the linearity of a large-sized device response. In fact, the displacement response of a large-sized device is mainly concentrated in the peak frequency of the wave (see $P(z_{fl})(f_w)$ in Table 4). So, despite the considerable energy dissipation, the large-sized device response is linear. This may be related to the fact that the internal-reaction specific frequency of the large-size devices f_{int} (see Table 1) is close to the peak frequency of the incident wave $f_w = 0.197$ Hz.

Instead, the medium-sized cases M3240, M6465 and M9250 induce a significant increase of the forcing wave, showing a direct dependence from the mass (see J^* at upstream gauge in Fig. 4), even if the forcing-wave drop downstream the device is lower than those of the large-sized cases (see $J^* > 0.6$ at downstream gauges in Fig. 4). This entails that the medium-sized devices not only dissipate the wave forcing, but also affect the wave characteristics in their vicinity. The combination of these effects induces an apparently linear response (see $RAO \simeq 1$ and $NLRAO < 0.25$ in Table 4), but this is not due to an ideal linear response of a medium-sized device. In fact, the internal-reaction specific frequency of the medium-sized devices is in the range $f_{int} = 0.5$–0.9 Hz, which is quite different from the peak frequency of the wave and this does not promote a linear response. The fact that this linearity is only apparent is confirmed by the RAO for the floater force (see Table 5). In large-sized test, the linear force contribution is greater than the nonlinear one ($RAO_F > NLRAO_F$), while in medium-sized devices we can find $RAO_F \simeq 0$ N/m. These zero values of RAO_F indicate that, in terms of power (which can be estimated as the product of time-derived displacement by the force), the response of the medium-sized devices is strongly nonlinear.

In the tests with small-sized devices, the evolution of the forcing wave is similar to that found in the tests with medium-sized devices, *i.e.* it increases upstream of the device (see $J^* \sim 1$–1.7 at gauge C1 in Fig. 5), while it is dissipated the downstream the device, where $J^* \sim 0.4$–0.9 (see downstream gauges in Fig. 5). This suggests that even small-sized devices have an apparently linear behaviour like medium-sized ones, although in this case some nonlinearity is highlighted by the linear RAOs differing from the unity (see $RAO \sim 0.75$–0.80 in Table 4).

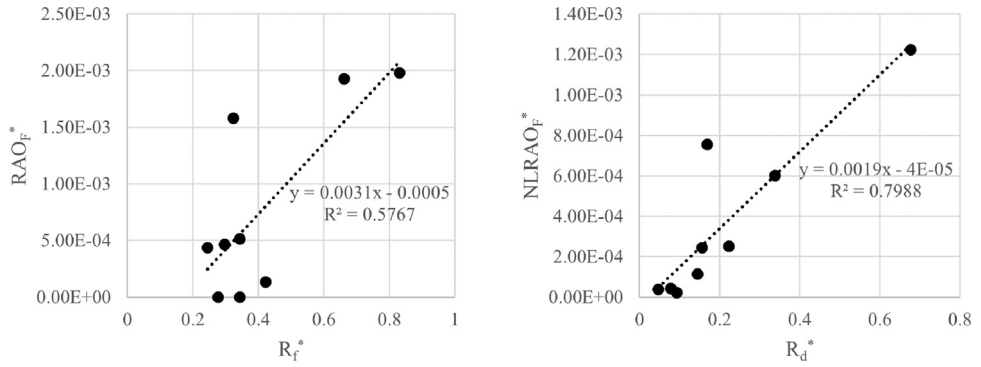

Fig. 7. RAO_F^* vs R_f^* (left panel), and $NLRAO_F^*$ vs R_d^* (right panel). The dashed line shows the linear trend reported in Eq. (10), where y is the response amplitude operator and x is the dimensionless freeboard or draft, accordingly to the panel content.

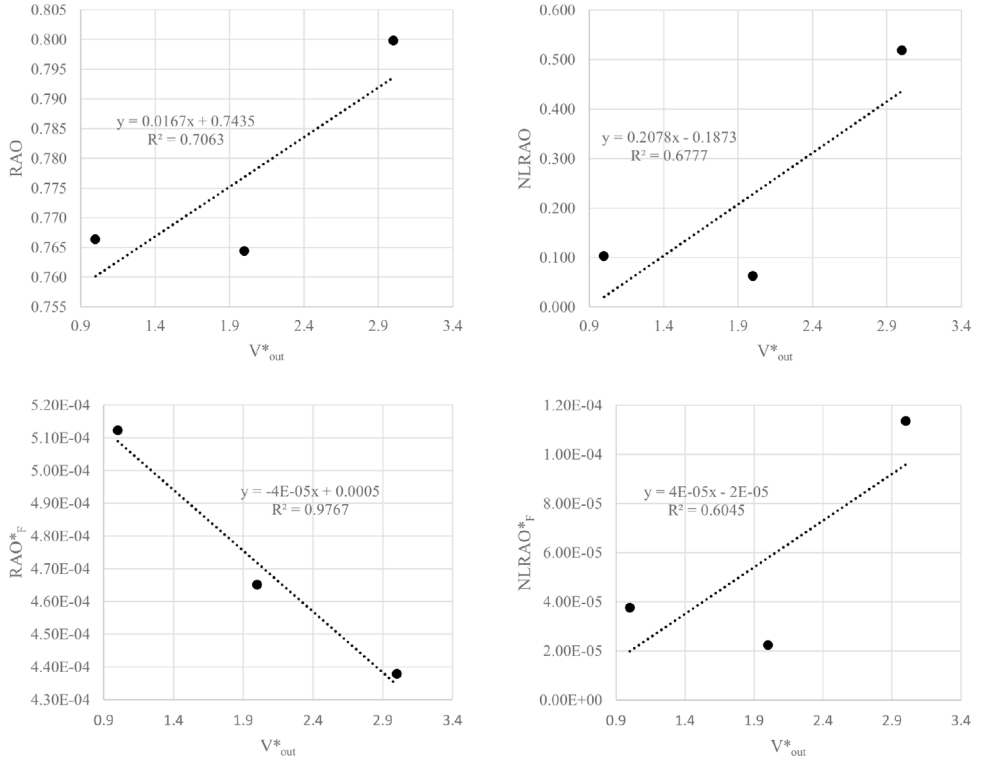

Fig. 8. RAO vs V_{out}^*. The dashed line shows the linear trend reported in the equation where y is the response amplitude operator and x is the volume of air under the floater.

In general, looking at the RAOs for both the floater displacement and force, we can say that the behaviour of small-sized devices is intermediate between large-sized ones (linear) and the medium-sized ones (only apparently linear), although the internal-reaction specific frequency of the devices is far from the peak frequency of the wave ($f_{int} \sim 0.5$–0.75 Hz).

The intermediate behaviour of small-sized devices is associated to an intense motion of the device out of the water (see $V_{out}^* \sim 0.9$–1.1 in Table 6) which is negligible in the other cases. To quantitatively assess the effect of out-of-the-water motion on the nonlinearity of the device response, Fig. 8 shows the RAO for both the floater displacement and force with respect to V_{out}^*. All RAOs show a growing linear dependence from the intensity of the out-of-the-water motion V_{out}^*, except for the linear contribution of the force RAO_F, which has a decreasing trend.

The displacement response is clearly related to the out-of-the-water motion of the floater, both in linear and nonlinear terms. The fact that the RAO increases with V_{out}^* is intuitive, since increasing the displacement of the device increases the amount of air volume that can be under it, for the same incident wave. Similarly, increasing the out-of-the-water motion reduces the surface area of water acting on the floater by decreasing the force response, *i.e.* decreasing RAO_F. Of particular interest is the linear relation between the out-of-the-water motion V_{out}^* and the nonlinear contributions of the $NLRAO$ and $NLRAO_F$. This relationship tells us that the nonlinearity of the response is directly proportional to the out-of-water motion of the device.

As mentioned for the results of Table 6, the overtopping volume V_{over}^* decreases with increasing floater size and increases with the mass/density increase, except for the cases of large-sized devices, where the effect of the mass/density appears negligible in generating the overtopping. To analyse how the overtopping volume affects the device response, the RAOs are illustrated in Fig. 9 with respect to V_{over}^*. The coefficients of determination are not suitable to support the validity of the proposed quantitative relationship, but acceptable to qualify an increasing trend of RAO and $NLRAO$ with respect to V_{over}^* and a decreasing trend of RAO_F and $NLRAO_F$ with respect to V_{over}^*.

The latter trend is easily explained: the presence of an overtopping volume induces a downward thrust on the floater, which partially

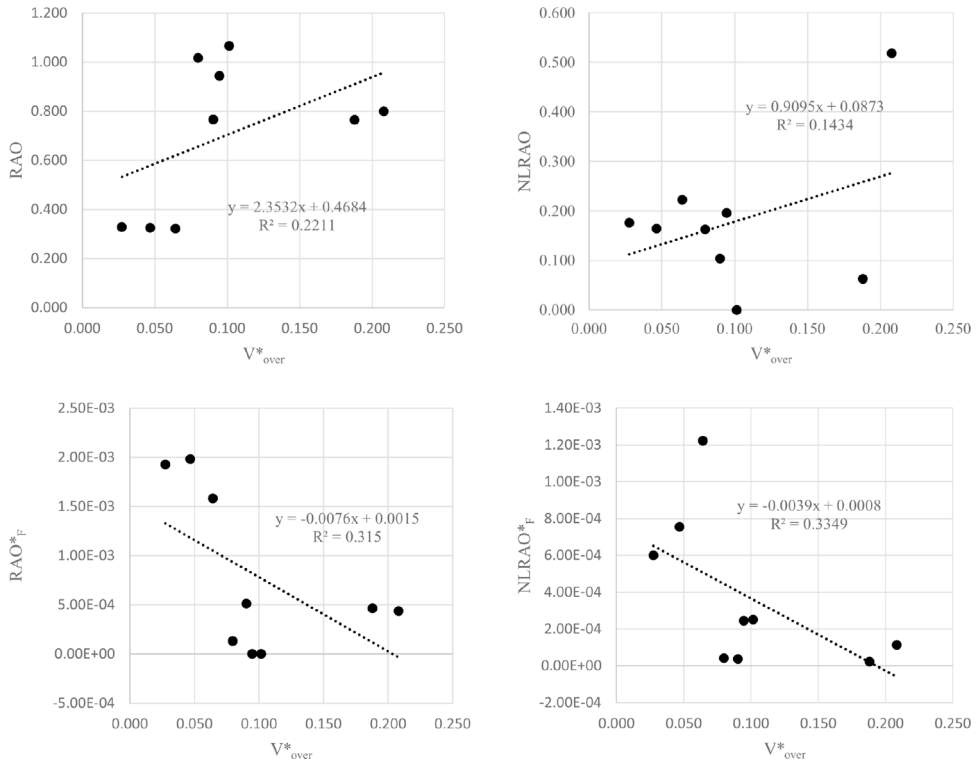

Fig. 9. RAO vs V^*_{over}. The dashed line shown the linear trend reported in the equation where y is the response amplitude operator and x is the overtopping volume.

balances the upward thrust due to the wave. This reduces the resultant force on the device, both in linear contributions RAO_F and in nonlinear contributions $NLRAO_F$. On the other hand, a reduction of the upward thrust should imply a reduction of the floater displacement, but this is not true, as shown by the increasing trend of the RAO, with a very low coefficient of determination. Subsequently, despite the overtopping generates a reduction in the force acting on the device, it does not affect significantly its displacement.

5. Conclusions

The sea states of the Adriatic Sea are less energetic than those of open oceans, being the most frequent ones characterized by a significant wave height lower than two metres and a peak period lower than eight seconds. On the other hand, the Adriatic Sea is rich in offshore infrastructure that can constitute hubs for various types of activities requiring electricity, which can be conveniently supplied with WEC devices. For this reason, the dynamic response of a SRPA is studied, considering a representative forcing wave of the Adriatic Sea, and varying the inertial characteristics of the device, *i.e.* size and density/mass, to identify the sources of possible nonlinear responses. This study, not including the control acting through the PTO subsystem, provides indications for a preliminary dimensioning of the device in the Adriatic Sea. The analysis of the dynamics obtained for different sizes of the device showed that:

- To maximize the linear response of the floater, its density should be minimized, and an optimal value of the floater thickness should be sought within the technological limits of this minimization.
- Large devices $D_{fl}/H_w \simeq 5$ induce considerable wave dissipation, but the dominant response is anyway linear;
- Medium-sized devices $D_{fl}/H_w \simeq 2.5$ have an apparently linear response, since the linear response in terms of displacement correspond to a nonlinear response in terms of acting forces;
- Small devices $D_{fl}/H_w \simeq 1.3$ exhibit an intermediate behaviour between the two described above, associated with a not-negligible out-of-the-water motion, which is directly proportional to the nonlinear responses of the device.

Instead, the mass seems to play a secondary role in affecting the nonlinearity of the response compared to the size, as it was found to only have an effect in favouring the wave overtopping, which reduces the forces acting on the floater, without affecting significantly the displacement. Although these conclusions are limited by the range of the explored parameters, and in particular by the unique definition of the PTO action, they provide important insight for the choice of the size of a device to be used in the Adriatic Sea, and for possible parameterization of the RAOs, which is necessary to manage the PTO control actions.

List of abbreviations

CFD: Computational Fluid dynamics;
FFT: Fast Fourier Transform;
NLRAO: NonLinear Response Amplitude Operator;
NREL: National Renewable Energy Laboratory;
OPT: Ocean Power Technologies;
PB3: PowerBuoy 3;
PTO: Power-Take-Off;
RAO: Response Amplitude Operator;
RANS: Reynolds Averaged Navier–Stokes;
RM3: Third reference model;
SDEWES: Sustainable Development of Energy Water and Environment System;
SRPA: Self-Reacting Floating Point Absorber;
VOF: Volume of Fluid;
WEC: Wave Energy Converter.

CRediT authorship contribution statement

Gianluca Zitti: Writing – review & editing, Writing – original draft, Visualization, Validation, Software, Methodology, Investigation, Formal analysis, Data curation, Conceptualization. **Maurizio Brocchini:** Supervision, Project administration, Funding acquisition, Formal analysis, Conceptualization.

Declaration of competing interest

The authors declare that they have no known competing financial interests or personal relationships that could have appeared to influence the work reported in this paper.

Acknowledgements

This study was carried out in the framework of the project PLaCE (PON Ricerca e In-novazione 2014–2020, project code: ARS01_00891, website: https://bluegrowth-place.eu/), co-funded by the European Union. The financial support of the PRIN 2022 project "NonlinEar Phenomena in floaTing offshore wind tUrbiNEs (NEPTUNE)", prot. 2022W7SKTL, funded by the Italian MUR and European Union – Next Generation EU, is greatly acknowledged.

A shorten version of this research has been presented during the 18th Conference on Sustainable Development of Energy Water and Environment System (SDEWES) held in Dubrovnik, Croatia, September 24–29, 2023. The title of the conference paper was "The Role of Size and Inerta on the Hydrodynamics of a Self-Reacting Two-Body Heave Single Point Absorber Wave Energy Converter".

Appendix A. Supplementary data

Supplementary material related to this article can be found online at https://doi.org/10.1016/j.renene.2024.120686.

References

[1] J.P. Kofoed, P. Frigaard, E. Friis-Madsen, H.C. Sørensen, Prototype testing of the wave energy converter wave Dragon, Renew. Energy 31 (2) (2006) 181–189, http://dx.doi.org/10.1016/j.renene.2005.09.005.

[2] K. Ahn, D. Truong, H.H. Tien, J.I. Yoon, An innovative design of wave energy converter, Renew. Energy 42 (2012) 186–194, http://dx.doi.org/10.1016/j.renene.2011.08.020.

[3] D.Q. Truong, K.K. Ahn, Development of a novel point absorber in heave for wave energy conversion, Renew. Energy 65 (2014) 183–191, http://dx.doi.org/10.1016/j.renene.2013.08.028.

[4] A.F. Falcão, J.C. Henriques, Oscillating-water-column wave energy converters and air turbines: A review, Renew. Energy 85 (2016) 1391–1424, http://dx.doi.org/10.1016/j.renene.2015.07.086.

[5] M. Chung, K.-Y. Shin, D.-S. Jeoune, S.-Y. Park, W.-J. Lee, Y.-H. Im, Economic evaluation of renewable energy systems for the optimal planning and design in Korea – a case study, J. Sustain. Dev. Energy Water Environ. Syst. 6 (4) (2018) 725–741, http://dx.doi.org/10.13044/j.sdewes.d6.0216.

[6] L. Martinelli, M. Volpato, C. Favaretto, P. Ruol, Hydraulic experiments on a small-scale wave energy converter with an unconventional dummy Pto, Energies 12 (7) (2019) 1218, http://dx.doi.org/10.3390/en12071218.

[7] A. Babarit, Potential: Energy resource and markets, in: Wave Energy Conversion, Elsevier, 2017, pp. 1–35, http://dx.doi.org/10.1016/b978-1-78548-264-9.50001-x.

[8] G. Besio, L. Mentaschi, A. Mazzino, Wave energy resource assessment in the Mediterranean sea on the basis of a 35-year hindcast, Energy 94 (2016) 50–63, http://dx.doi.org/10.1016/j.energy.2015.10.044.

[9] G. Mattiazzo, State of the art and perspectives of wave energy in the Mediterranean sea: Backstage of ISWEC, Front. Energy Res. 7 (2019) http://dx.doi.org/10.3389/fenrg.2019.00114.

[10] A. Miquel, A. Lamberti, A. Antonini, R. Archetti, The MoonWEC, a new technology for wave energy conversion in the mediterranean sea, Ocean Eng. 217 (2020) 107958, http://dx.doi.org/10.1016/j.oceaneng.2020.107958.

[11] D. Curto, V. Franzitta, M. Trapanese, M. Cirrincione, A preliminary energy assessment to improve the energy sustainability in the small Islands of the Mediterranean sea, J. Sustain. Dev. Energy Water Environ. Syst. 8 (4) (2020) 735–753, http://dx.doi.org/10.13044/j.sdewes.d7.0314.

[12] L. Ciappi, L. Cheli, I. Simonetti, A. Bianchini, L. Talluri, L. Cappietti, G. Manfrida, et al., Analytical models of oscillating water column systems operating with air turbines in the Mediterranean sea, in: Proceedings of the 15th Conference on Sustainable Development of Energy, Water and Environment Systems, SDEWES, SDEWES, 2020, pp. 1–20.

[13] G. Lavidas, K. Blok, Shifting wave energy perceptions: The case for wave energy converter (WEC) feasibility at milder resources, Renew. Energy 170 (2021) 1143–1155, http://dx.doi.org/10.1016/j.renene.2021.02.041.

[14] C. Lo Re, G. Manno, M. Basile, G. Ciraolo, The opportunity of using wave energy converters in a Mediterranean hot spot, Renew. Energy 196 (2022) 1095–1114, http://dx.doi.org/10.1016/j.renene.2022.07.010.

[15] I. Martić, N. Degiuli, C.G. Grlj, Scaling of wave energy converters for optimum performance in the Adriatic sea, Energy 294 (2024) 130922, http://dx.doi.org/10.1016/j.energy.2024.130922.

[16] J.T. Claisse, D.J. Pondella, M. Love, L.A. Zahn, C.M. Williams, A.S. Bull, Impacts from partial removal of decommissioned oil and gas platforms on fish biomass and production on the remaining platform structure and surrounding shell mounds, in: J.P. Meador (Ed.), PLOS ONE 10 (9) (2015) e0135812, http://dx.doi.org/10.1371/journal.pone.0135812.

[17] D.J. Pondella, L.A. Zahn, M.S. Love, D. Siegel, B.B. Bernstein, Modeling fish production for southern California's petroleum platforms, Integr. Environ. Assess. Manag. 11 (4) (2015) 584–593, http://dx.doi.org/10.1002/ieam.1689.

[18] B. Sommer, A.M. Fowler, P.I. Macreadie, D.A. Palandro, A.C. Aziz, D.J. Booth, Decommissioning of offshore oil and gas structures – environmental opportunities and challenges, Sci. Total Environ. 658 (2019) 973–981, http://dx.doi.org/10.1016/j.scitotenv.2018.12.193.

[19] M. Leporini, B. Marchetti, F. Corvaro, F. Polonara, Reconversion of offshore oil and gas platforms into renewable energy sites production: Assessment of different scenarios, Renew. Energy 135 (2019) 1121–1132, http://dx.doi.org/10.1016/j.renene.2018.12.073.

[20] G. Zitti, N. Novelli, M. Brocchini, Preliminary results on the dynamics of a pile-Moored fish cage with elastic net in currents and waves, J. Mar. Sci. Eng. 9 (1) (2020) 14, http://dx.doi.org/10.3390/jmse9010014.

[21] G. Colaleo, P. Contestabile, T. Bellezze, L. Margheritini, A. Dell'Anno, D. Vicinanza, Prototype experiments of the low voltage mineral deposition technology as eco-friendly solution for improving the sustainability of offshore platforms at the end of their production life, Environ. Technol. Innov. 27 (2022) 102412, http://dx.doi.org/10.1016/j.eti.2022.102412.

[22] G. Zitti, N. Novelli, M. Brocchini, Dynamics of a pile-moored fish cages in current and waves: A numerical study, Ocean Eng. 269 (2023) 113571, http://dx.doi.org/10.1016/j.oceaneng.2022.113571.

[23] F. Zugno, R. Schiavon, I. Zanino, A. Alessi, A. Giuggioli, A. Malkowski, M. Tedaldi, L. Di Vito, A. Dell'Anno, PLaCE - A Case Study of an Offshore Asset Conversion for Multiple Eco-Sustainable Re-Use in the Adriatic Sea, in: Offshore Mediterranean Conference and Exhibition, vol. All Days, 2021, arXiv:https://onepetro.org/OMCONF/proceedings-pdf/OMC21/All-OMC21/OMC-2021-053/2529913/omc-2021-053.pdf. OMC-2021-053.

[24] Ocean Power Technologies, Inc, Ocean Power Technologies Ships PB3 PowerBuoy to Eni S.p.A for Deployment in Adriatic Sea, Ocean Power Technologies, Inc, 2018, URL https://investors.oceanpowertechnologies.com/node/11386/pdf.

[25] A. Alessi, E. Boi, A. Malkowski, C. Cesari, B. Cresci, F. Zanon, G. Rana, F. Furlan, E. De Marchi, R. Schiavon, K. Parsa, P. Watson, Application of wave energy converter technology to subsea power requirements and asset integrity in oil and gas field developments, in: Offshore Mediterranean Conference and Exhibition, 2019, arXiv:https://onepetro.org/OMCONF/proceedings-pdf/OMC19/All-OMC19/OMC-2019-1032/1134932/omc-2019-1032.pdf. OMC-2019-1032.

[26] J. van Rij, Y.-H. Yu, K. Edwards, M. Mekhiche, Ocean power technology design optimization, Int. J. Mar. Energy 20 (2017) 97–108, http://dx.doi.org/10.1016/j.ijome.2017.07.010.

[27] S.J. Beatty, M. Hall, B.J. Buckham, P. Wild, B. Bocking, Experimental and numerical comparisons of self-reacting point absorber wave energy converters in regular waves, Ocean Eng. 104 (2015) 370–386, http://dx.doi.org/10.1016/j.oceaneng.2015.05.027.

[28] S.J. Beatty, B. Bocking, K. Bubbar, B.J. Buckham, P. Wild, Experimental and numerical comparisons of self-reacting point absorber wave energy converters in irregular waves, Ocean Eng. 173 (2019) 716–731, http://dx.doi.org/10.1016/j.oceaneng.2019.01.034.

[29] Y.-H. Yu, Y. Li, Reynolds-averaged Navier–Stokes simulation of the heave performance of a two-body floating-point absorber wave energy system, Comput. Fluids 73 (2013) 104–114, http://dx.doi.org/10.1016/j.compfluid.2012.10.007.

[30] V. Neary, Y.-H. Yu, J. Epler, K. Shoele, M. Previsic, M. Lawson, Y. Li, Reference model 3 scaled geometry (RM3: Wave point absorber), in: Marine and Hydrokinetic Data Repository, MHKDR, Sandia National Laboratories, 2014, http://dx.doi.org/10.15473/1818910.

[31] K. Ruehl, C. Michelen, S. Kanner, M. Lawson, Y.-H. Yu, Preliminary verification and validation of WEC-sim, an open-source wave energy converter design tool, in: Volume 9B: Ocean Renewable Energy, in: OMAE2014, American Society of Mechanical Engineers, 2014, http://dx.doi.org/10.1115/omae2014-24312.

[32] Q. Xu, Y. Li, Y.-H. Yu, B. Ding, Z. Jiang, Z. Lin, B. Cazzolato, Experimental and numerical investigations of a two-body floating-point absorber wave energy converter in regular waves, J. Fluids Struct. 91 (2019) 102613, http://dx.doi.org/10.1016/j.jfluidstructs.2019.03.006.

[33] K. Mahmoodi, H. Ghassemi, A. Razminia, Performance assessment of a two-body wave energy converter based on the Persian Gulf wave climate, Renew. Energy 159 (2020) 519–537, http://dx.doi.org/10.1016/j.renene.2020.06.071.

[34] O.M. Faltinsen, Sea loads on floating offshore systems, 1993, http://dx.doi.org/10.4043/7142-ms.

[35] A. Amiri, R. Panahi, S. Radfar, Parametric study of two-body floating-point wave absorber, J. Mar. Sci. Appl. 15 (1) (2016) 41–49, http://dx.doi.org/10.1007/s11804-016-1342-1.

[36] C. Liang, L. Zuo, On the dynamics and design of a two-body wave energy converter, Renew. Energy 101 (2017) 265–274, http://dx.doi.org/10.1016/j.renene.2016.08.059.

[37] Q.-L. Xu, Y. Li, Z.-L. Lin, An improved boundary element method for modelling a self-reacting point absorber wave energy converter, Acta Mech. Sinica 34 (6) (2018) 1015–1034, http://dx.doi.org/10.1007/s10409-018-0792-x.

[38] Y. Li, Y.-H. Yu, J. Epler, M. Previsic, Experimental investigation of the power generation performance of floating-point absorber wave energy systems, 2012, URL https://www.osti.gov/biblio/1040938.

[39] ANSYS, ANSYS fluent tutorial guide inc. Release 18.0, 2017.